nature energy

Article

https://doi.org/10.1038/s41560-025-01907-5

Grid-scale corrosion-free Zn/Br flow batteries enabled by a multi-electron transfer reaction

Received: 4 June 2025

Accepted: 16 October 2025

Published online: 19 December 2025

Check for updates

Yue Xu[1,2,3], Tianyu Li[1,3], Zhangquan Peng[4], Congxin Xie[1,3] ✉ & Xianfeng Li[1,3] ✉

Flow batteries are promising for renewable energy storage due to their safety and scalability. Zinc/bromine flow batteries (Zn/Br) are popular due to their high energy densities and inexpensive electrolytes. However, they have a poor service life and lead to environmental harm as a result of the generated corrosive and volatile Br_2. Here we introduce a Br_2 scavenger to the catholyte, reducing the Br_2 concentration to an acceptable level (~7 mM). The scavenger, sodium sulfamate (SANa), reacts rapidly with Br_2 to form a mild product, *N*-bromo sodium sulfamate (Br-SANa; Br^+). Additionally, the two-electron transfer reaction of Br-SANa/Br^- (Br^+/Br^-) increases the energy density. We have developed a Zn/Br flow battery, paired with a Zn anode, that outperforms traditional Zn/Br flow batteries in energy density (152 Wh l^{-1} versus 90 Wh l^{-1}) and cycle life (>600 versus 30 cycles), using a sulfonated polyetheretherketone membrane. We assembled a 5-kW stack that operated stably for over 700 cycles (~1,400 h). Using this reaction, we have built a large-scale battery system.

Bromine (Br_2) corrosion raises the stringent requirements for battery components in current bromine-based flow batteries (FBs)[1], as it reduces the stability and lifetime of the electrodes and membranes, and even of auxiliary equipment such as pipelines and electrolyte tanks[2]. Br_2 oxidizes and pulverizes common carbon-based electrodes and bipolar plates into carbon oxides[3,4], and breaks polymer chains through side reactions such as addition (for example, C=C bonds) or substitution (for example, ether bonds)[5]. For these reasons, state-of-the-art Zn/Br FBs are extensively equipped with corrosion-resistant components such as Nafion or polyolefin membranes and polyvinylidene fluoride (PVDF) pipes and tanks[6]. Besides being corrosive, Br_2 is also highly volatile (boiling point of only 58 °C) and toxic. When released, it pollutes the atmosphere, corrodes human skin and mucous membranes, and stimulates the central nervous system[7,8].

To alleviate this corrosion and other harmful effects of Br_2, current bromine-based batteries use complexing agents to capture free Br_2 in the catholyte[9]. These agents, which are typically quaternary ammonium salts such as 1-ethyl-1-methylpyrrolidinium bromide (MEP), form oily precipitates with Br_2 (MEP-Br_2)[10,11]. The problem of this strategy is that the concentration of free Br_2 is still high, at up to hundreds of millimoles per litre of electrolyte, and the capture is done at the expense of kinetics from phase separation[12] and higher cost. Oily Br_2 precipitates affect mass transfer, and an uneven distribution of oily Br_2 on the electrodes affects the stability of the batteries[13]. Corrosion by the oily Br_2 cannot be ignored, so there is an urgent need for reactions and/or strategies to mitigate the negative effects of free Br_2.

In this Article we report a bromine reaction that almost completely eliminates Br_2 corrosion. We introduce a Br_2 scavenger, sodium sulfamate (SANa), into the catholyte. This can dramatically decrease the Br_2 concentration to an acceptable level (~7 mM). SANa reacts rapidly with Br_2 as it forms during charging, producing a mild product, *N*-bromo sodium sulfamate (Br-SANa; Br^+). During discharge, Br-SANa participates in the reaction by dissociating into Br_2 through chemical equilibrium. In addition, the two-electron transfer reaction of Br-SANa/Br^- (Br^+/Br^-) increases the battery energy density. A Zn/Br FB assembled using this electrolyte as well as regular, inexpensive sulfonated

[1]Division of Energy Storage, Dalian Institute of Chemical Physics, Chinese Academy of Sciences, Dalian, China. [2]University of Chinese Academy of Sciences, Beijing, China. [3]Key Laboratory of Long-Duration and Large-Scale Energy Storage (Chinese Academy of Sciences), Beijing, China. [4]Laboratory of Advanced Spectro-electrochemistry and Li-ion Batteries, Dalian Institute of Chemical Physics, Chinese Academy of Sciences, Dalian, China. ✉e-mail: xiecongxin@dicp.ac.cn; lixianfeng@dicp.ac.cn

polyetheretherketone (SPEEK) membranes (which are not resistant to corrosion) outperformed a traditional Zn/Br FB in terms of energy density (152 Wh l^{-1} versus 90 Wh l^{-1}) and cycle life (>600 cycles versus <30 cycles) with an energy efficiency (EE) of 82% at a current density of 40 mA cm^{-2}. Most importantly, we assembled a 5-kW system that delivers an output of 6.6 kWh, achieving an EE of 78%. Furthermore, the assembled 5-kW stack was able to operate for over 700 cycles (or 1,400 h) at 40 mA cm^{-2}, demonstrating its practicality.

Building a molecular library of Br_2-scavenging agents

It is recognized that certain organic amines react with Br_2 to form bromoamino reagents (BrNs) (equation (1))[5,14]. Unlike a traditional complexing reaction[15], this reaction forms a $Br^{\delta+}$–$N^{\delta-}$ covalent bond and eliminates free Br_2 species during the reaction process[16,17]. It is fundamentally a disproportionation reaction, where Br_2 undergoes disproportionation to form both Br^+ and Br^-. Then Br^+ electrophilically replaces the hydrogen on the amino group to form BrNs, and a proton is generated at the same time. Inspired by this reaction, we conceived a reaction comprising introducing amino-containing compounds into the electrolyte as scavengers to eliminate Br_2. During charging, bromide ions (Br^-) are electrochemically oxidized to Br_2, which can rapidly substitute the hydrogen on the amino group of the scavenger to form BrNs products, along with Br^- and protons (Fig. 1a). This is a chemical equilibrium process, and the remaining amount of Br_2 in the electrolyte depends on the equilibrium constant of the substitution reaction. Meanwhile, the generated Br^- can further participate in the electrochemical charging process. During discharge, BrNs dissociate into Br_2 through a chemical equilibrium to participate in the discharge reaction. Because the stability of BrNs depends on the strength of the Br–N bond, which, in turn, is related to the electron cloud density on the N of the scavenger, we theoretically calculated the effects of various electron-withdrawing/donating groups (EWGs/EDGs) linked to -NH on the strength of the resultant Br–N bonds.

By screening various EWGs and EDGs, we found that EWGs lead to stronger Br–N bonds than EDGs (Fig. 1b), because EWGs reduce the electron cloud density of the N and facilitate proton departure and bromination (equation (2)). EDGs, on the other hand, enhance the electron cloud density of N and discourage the formation of desired $Br^{\delta+}$–$N^{\delta-}$ moieties (equation (3)). For BrNs with overly strong EWGs, such as hydrogen bis(fluorosulfonyl)imide (HFSI), however, the hydrogen on the -NH moiety ($pK_a < 2$, where pK_a is the negative logarithm of the acid dissociation constant K_a) spontaneously leaves in the form of a proton, making it impossible to form Br–N covalent bonds (Fig. 1b). These results show that for our designed reaction to proceed, we need to identify EWGs to facilitate the formation of the Br–N bond, but which are not so strong that the -NH group on the scavenger is completely ionized.

To identify a suitable scavenger, we screened 17 amino compounds with different EWGs (Supplementary Table 1) and performed cyclic voltammetry measurements on them in a nearly neutral environment (Supplementary Fig. 1). The intensity of the electron-withdrawing effect determines the ease with which the proton leaves the amino group, represented by the pK_a value. Based on variations in the pK_a value, we categorize the strength of the electron-withdrawing effect into three levels: strong, moderate and weak (Supplementary Table 1). Compared with pristine NaBr electrolyte, electrolytes containing scavengers displayed higher oxidation peak currents that were roughly inversely proportional to the pK_a of the scavengers (yellow and blue regions, Fig. 1c). The smaller the pK_a, the easier it is for protons to leave and bromination reaction to occur. However, for overly strong EWGs (green region, Fig. 1c) ($pK_a < 2$), no obvious oxidation peak enhancement was observed due to the spontaneous dissociation of the proton from the -NH groups. Of all the scavengers examined, SANa displayed the highest oxidation peak current, which means it has the highest bromination reaction rate.

Effect of pH on bromination

Besides the pK_a of the scavenger, the pH of the electrolyte also substantially affects the redox potential of the proton-coupled bromination reaction. In a strongly acidic environment (pH of ~0), electrochemical oxidation of Br^- in the presence of SANa showed two separated oxidation peaks that corresponded to two successive electrochemical processes (Supplementary Fig. 2). Br^- was electrochemically oxidized to Br_2 in step 1 (equation (4)), followed by electrochemical conversion of Br_2 to Br–SANa in step 2 (equation (5)). In this case, the strongly acidic electrolyte does not support the designed working principle of a Br_2-scavenging reaction, because it will accumulate a large amount of Br_2 in step 1. When the electrolyte pH was gradually increased (Supplementary Fig. 3), however, the redox potential of step 2 dropped and gradually overlapped with step 1. In thermodynamics, spontaneous chemical reactions can only occur (equation (6)) if the potential of step 2 (equation (5)) is lower than that of step 1 (equation (4)). This can be validated by the reaction between Br_2 and SANa (Supplementary Fig. 4). Under neutral conditions, as SANa is added, the colour of the red Br_2 gradually lightens, indicating that Br_2 and SANa are forming a Br–SANa compound through a chemical reaction. Therefore, ensuring the electrolyte is at an appropriate pH guarantees a spontaneous reaction.

$$R(R') - NH_2 + Br_2 \rightleftharpoons R(R') - NH - Br + Br^- + H^+ \quad (1)$$

Electron cloud

$$\mathbf{EWG}\text{—}NH\text{--}H + Br_2 \rightleftharpoons EWG\text{—}\overset{\delta^-}{N}H\text{—}\overset{\delta^+}{Br} + Br^- + H^+ \quad (2)$$

Electron cloud

$$\mathbf{EDG}\text{—}NH\text{—}H + Br_2 \not\rightleftharpoons EDG\text{—}\overset{\delta^-}{N}H\text{—}\overset{\delta^+}{Br} + Br^- + H^+ \quad (3)$$

$$2Br^- - 2e^- \rightarrow Br_2 \quad (4)$$

$$NH_2 - SO_3^- + 1/2Br_2 - e^- \overset{\text{Strongly acidic}}{\rightleftharpoons} Br - \overset{H}{N} - SO_3^- + H^+ \quad (5)$$

$$NH_2 - SO_3^- + Br_2 \overset{\text{Nearly neutral}}{\rightleftharpoons} Br - \overset{H}{N} - SO_3^- + Br^- + H^+ \quad (6)$$

After reaching chemical equilibrium, the concentration of the remaining Br_2 was inversely proportional to the electrolyte pH (Supplementary Fig. 5). When the pH of the electrolyte reached ~2.1, the concentration of free Br_2 in a 0.5 M SANa + 0.5 M Br_2 solution dropped to 10 mM. Further raising the pH to 3.1 reduced the residual Br_2 concentration to ~1 mM. This means that a weakly acidic/nearly neutral environment is necessary for the scavenger to substantially remove free Br_2. Therefore, to eliminate the impact of proton release from the amino group on the pH of the electrolyte, a buffer reagent such as acetate (HAc/Ac^-) needs to be used as a proton sink (for charge reaction) or source (for discharge reaction). The pH effect was further confirmed visually by the gradual lightening of the Br_2 + SANa electrolyte when potassium acetate (KAc) was added stepwise (Supplementary Fig. 6). As the concentration of KAc gradually increases, the concentration of Br_2 in the solution decreases accordingly (Supplementary Fig. 7). So far, the basic formula of the electrolyte has been reached, including at least Br^- as the active material, SANa as the scavenger and Ac^- as the buffer reagent.

Electrochemical and chemical mechanism

We investigated the charge/discharge mechanism of the electrolyte formulation at near-neutral pH. Cyclic voltammetry (CV) on a Pt electrode in electrolytes containing 10 mM SANa, 10 mM NaBr, 0.2 M $NaClO_4$ and various concentrations of KAc showed one oxidation and two reduction

https://doi.org/10.1038/s41560-025-01907-5

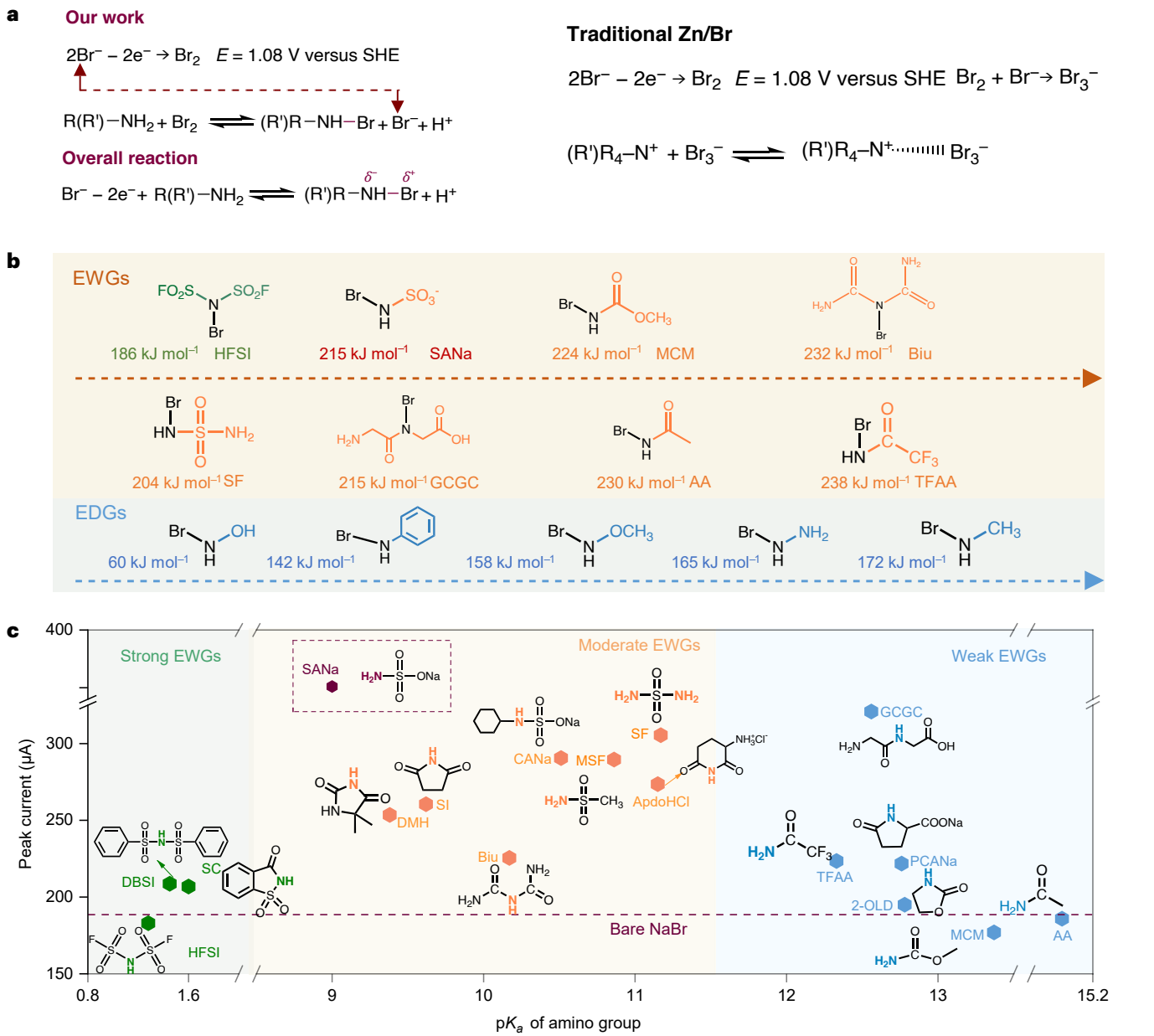

Fig. 1 | Design principles of bromine electrolytes. a, Schematic of an advanced FB (left) and a conventional (right) Zn/Br FB. Unlike the conventional electrochemical process of Br^-/Br_2, the electrochemically generated Br_2 further reacts with amines to form BrNs. **b**, Density functional theory-calculated Br–N bond energies for BrNs compounds with different EWGs and EDGs. Compounds with EWGs had stronger and more stable Br–N bonds than those with EDGs, because EWGs reduce the electron cloud density on the N, facilitating proton departure and bromination (equations (2 and 3)). **c**, Plot of peak current for 17 amino compounds with various EWGs as a function of the pK_a of the amino group. The peak current, which is related to bromination rate, is higher than for the pure NaBr electrolyte (dashed line) for most compounds and roughly inversely proportional to pK_a. This is because the lower the pK_a, the easier it is for the hydrogen on the amino group to leave, and the faster the bromination reaction rate is. However, a pK_a that is too low (<2) can cause the hydrogen on the -NH groups to spontaneously dissociate as a proton and prevent the formation of a Br–N bond.

peaks in the potential range of ~0.0–1.2 V versus saturated calomel electrode (SCE; Fig. 2a). $NaClO_4$, which is electrochemically inert at room temperature, was selected as the supporting electrolyte for CV tests under neutral pH conditions (Supplementary Fig. 8). The oxidation peak at 1.0 V was assigned to the electrooxidation of Br^- to Br_2 followed by the chemical reaction with SANa to produce Br–SANa (step 1). The reduction peak at ~0.8 V was assigned to the electroreduction of free Br_2 from the chemical equilibrium (step 2). As the concentration of KAc increases, the pH rises, resulting in a decrease in proton activity, making it difficult for Br–SANa to dissociate into Br_2. Therefore, Br–SANa can only be converted to Br^- through an electrochemical reduction reaction at ~0.4 V, which corresponds to step 3. Quantitative charge analysis of the CV curves showed that the increase in KAc substantially increased the proportion of step 3 (Supplementary Fig. 9). This means that the pathway of the reduction reaction depends on the pH of the electrolyte.

Because the HAc/Ac^- buffer solution stabilizes the electrolyte pH at ~5, we used Zn/Zn^{2+} as the anode to assemble a Zn/Br FB. The battery using this electrolyte formulation showed a pair of charge–discharge plateaux (Fig. 2b). Under the condition where the charge capacity reached 26.8 Ah l^{-1} at the end of charging, the concentration of Br_2 in the battery, measured by UV–vis spectroscopy, was ~7 mM (Fig. 2c and Supplementary Fig. 10). This concentration was notably lower than in

https://doi.org/10.1038/s41560-025-01907-5

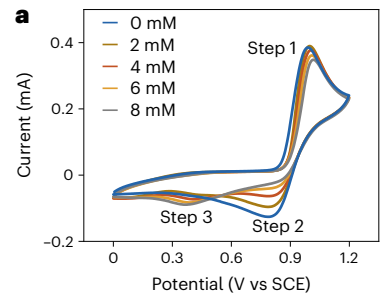

Step 1: $2Br^- - 2e^- \rightarrow Br_2$ E = 1.08 V vs SHE

$Br_2 + NH_2SO_3^- + Ac^- \rightarrow Br\text{-}NHSO_3^- + HAc + Br^-$

Step 2: $Br\text{-}NHSO_3^- + HAc + Br^- \rightarrow Br_2 + NH_2SO_3^- + Ac^-$

$Br_2 + 2e^- \rightarrow 2Br^-$ E = 1.08 V vs SHE

Step 3: $Br\text{-}NHSO_3^- + H_2O + 2e^- \rightarrow Br^- + NH_2SO_3^- + OH^-$

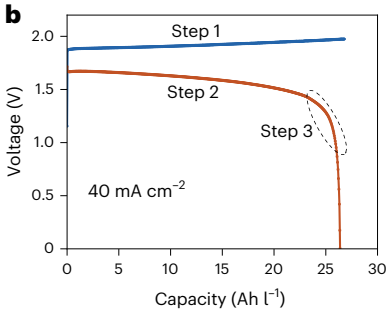

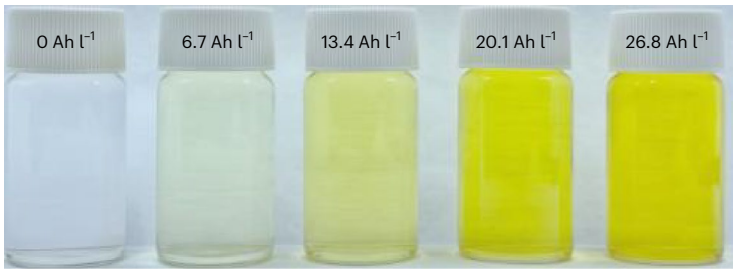

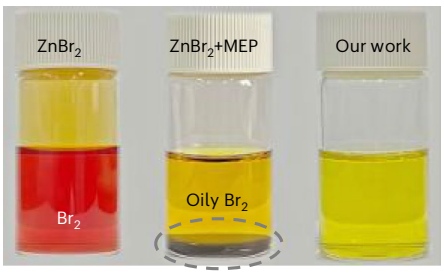

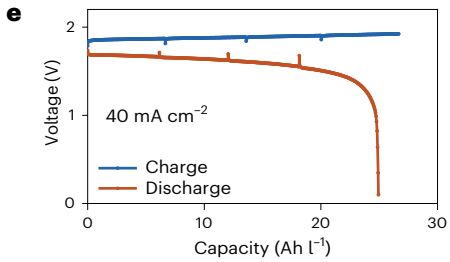

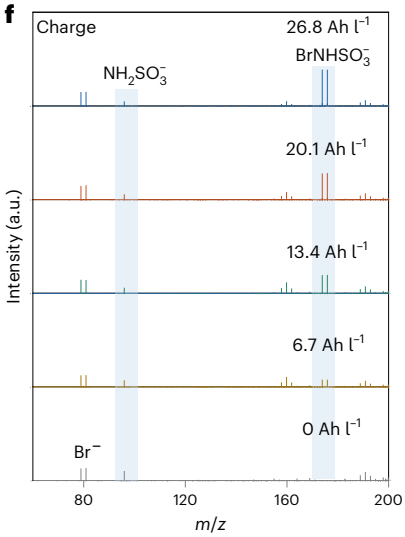

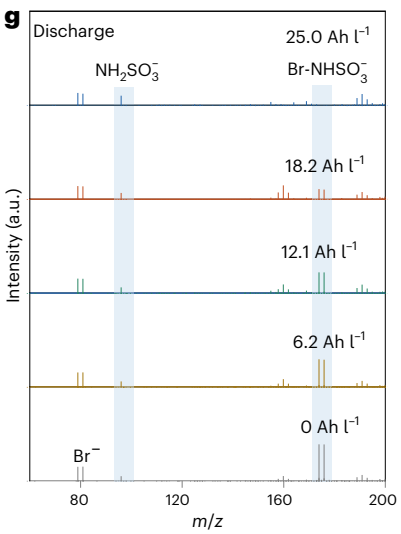

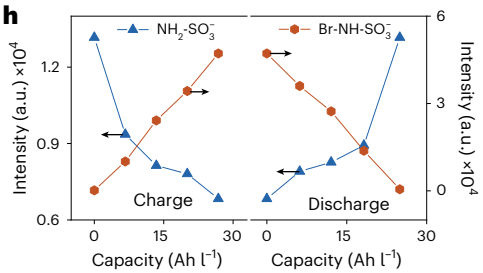

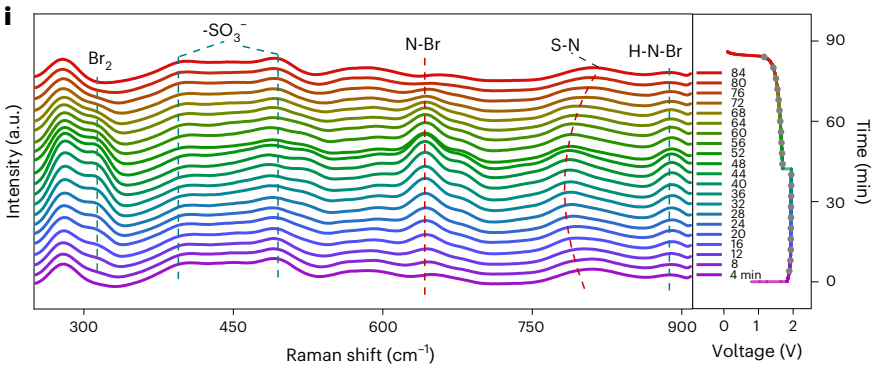

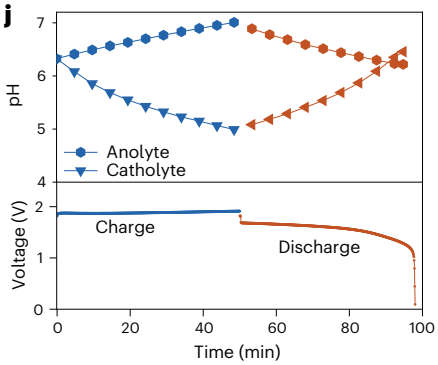

Fig. 2 | Electrochemistry of Br_2 in the presence of SANa. a, CV of a Pt electrode in an electrolyte solution of 10 mM NaBr + 10 mM SANa + 0.2 M $NaClO_4$ + x mM KAc. The corresponding electrochemical reaction equations are shown on the right. **b**, Charge–discharge curve of a flow battery assembled with a Zn anode and an electrolyte containing 1 M $ZnBr_2$ + 1 M SANa + 2 M KAc. **c**, Photographs of the electrolyte when the battery was charged to different capacities. The free Br_2 was ~7 mM at the end of the charge. **d**, Photographs of different bromine electrolytes at the end of the charge. Unlike the conventional bromine electrolyte (1 M $ZnBr_2$ + 3 M KCl) without (left) or with (middle) 0.3 M MEP, this electrolyte (right) had no oily Br_2-containing precipitates and had visibly less aqueous Br_2 species. **e**, Charge–discharge curve of a Zn/Br FB used for mass spectrometry sampling. Electrolyte composition: 1 M $ZnBr_2$ + 1 M SANa + 2 M KAc + 2 M KBr. **f**,**g**, As charging progressed (**f**), the Br–SANa signal increased and the SANa signal weakened. During discharge, the Br–SANa signal gradually disappeared, while the SANa signal enhanced, demonstrating its reversibility (**g**). The two blue-shaded bars represent the ion peaks of $NH_2SO_3^-$ and $Br\text{-}NHSO_3^-$. **h**, Intensity versus charge–discharge capacity plots derived from the mass spectrometric results presented in **f** and **g**. **i**, In situ Raman spectra of the catholyte during a full cycle of charge–discharge. Signals of the Br–N bond indicated the formation of BrNs compounds. **j**, Top: throughout the charge–discharge process, the pH of the electrolyte at both positive and negative sides remains within a range of pH 5–7. Bottom: representative charge–discharge curves.

the conventional electrolyte, where the concentration of free Br_2 was typically as high as 128 mM and accompanied by massive amounts of oily Br_2 precipitates (Fig. 2d, middle and Supplementary Fig. 11). The effect of SANa and pH on the electrochemical behaviour of the bromine-based electrolyte is further illustrated by the pH–potential phase diagram in Supplementary Fig. 12.

The reaction mechanism and reversibility were confirmed by electrospray ionization mass spectrometry (ESI-MS). During charging, ESI-MS analysis of the catholyte showed evolution of signals at m/z = 173.88 and 175.88, providing solid experimental evidence of the formation of Br–SANa ions ($Br–NHSO_3^-$; Fig. 2e,f). As charging proceeded, the Br–SANa signal increased, whereas the SANa signal weakened (Fig. 2h). During discharge, the Br–SANa signal gradually diminished and disappeared, whereas the SANa signal recovered (Fig. 2g,h), confirming the reversibility of the process. Further, proton NMR (^{1}H NMR) of the catholyte showed that the H on the N atom of SANa after bromination experienced a chemical shift to low field due to the electron-withdrawing effect of Br (Supplementary Fig. 13). Moreover, in situ Raman spectroscopy identified symmetric (643 cm^{-1}) and asymmetric stretching (680 cm^{-1}) of the Br–N bond that formed upon charging (Fig. 2i and Supplementary Fig. 14)[18,19]. Because the Br attached to N weakens the S–N bond strength, the S–N stretching vibration shifted from 815 cm^{-1} to 783 cm^{-1} as it charged[20]. The catholyte also displayed the stretching vibration[21,22] (310 cm^{-1}) of the Br_2 species from the chemical equilibrium of Br–SANa, which disappeared completely at the end of the discharge. The pH of the electrolyte remained within a near-neutral range (pH 5–7) throughout the electrochemical charge–discharge process (Fig. 2j). Compared to the strong fluctuations of pH of the electrolyte in traditional Zn/Br FBs (pH 3–6; Supplementary Fig. 15a), the pH in our electrolyte was more stable. In addition, due to the overall higher pH, the hydrogen evolution reaction is less than that of a traditional Zn/Br FB (Supplementary Fig. 15b). Surface-enhanced Raman spectroscopy (SERS) further proved that Br–SANa was produced by the chemical reaction of Br_2 and SANa (Supplementary Fig. 16)[23,24]. However, for strongly acidic electrolytes (pH of ~0), the signal of Br–SANa could only be observed in step 2 after Br^- was oxidized to Br_2 in step 1, and Br_2 electrochemically generated Br–SANa (Supplementary Fig. 17). Meanwhile, as the acid concentration in the electrolyte decreased, the potential difference between the first and second plateaux gradually decreased (Supplementary Fig. 18), indicating that the potential of the second plateau is related to proton concentration, consistent with previous CV results.

We also selected other scavengers such as trifluoromethanesulfonamide (TFMSF) for testing. Due to its lower pK_a value (6.37 versus the 9.00 of SANa), the protons on the amine group tend to dissociate, making the formation of brominated compounds more difficult. As a result, the concentration of free Br_2 in the electrolyte is notably higher than that of SANa (Supplementary Fig. 19).

Fitting the CV with an electrochemical–chemical (EC) reaction mechanism[25,26], the electron transfer rate constant and subsequent chemical reaction rate constant were found to be 1.212×10^{-2} cm s^{-1} and 99.35 M^{-1} s^{-1}, respectively (Supplementary Fig. 20). We linearly fitted log(Br_2/Br–SANa) as a function of pH of the prepared electrolyte solution to calculate the chemical equilibrium constant of the reaction of Br_2 and SANa. For the electrolyte without KAc, the equilibrium constant was measured to be 0.020 M. The equilibrium constant increased to 1,111 for electrolyte containing Ac^-. A large equilibrium constant indicates that the products predominate, and substantial bromination occurs in the electrolyte with Ac^- (Supplementary Fig. 21; see 'Thermodynamics calculations' for details).

Electrochemical performance of single and scaled-up systems

As a proof of concept, a single Zn/Br FB was assembled with this electrolyte design. Because the electrolyte is mild and neutral, we used a regular, low-cost SPEEK membrane that is not resistant to corrosion. The SPEEK membrane demonstrated high selectivity for Br–SANa (Supplementary Fig. 22). The flow of anolyte helps to reduce the concentration polarization of Zn^{2+}, thereby effectively inhibiting zinc dendrites. The specific capacity of the charge–discharge curves confirmed a two-electron transfer mechanism (Supplementary Fig. 23). The two-electron transfer process resulted in a much higher energy density than traditional Zn/Br FBs (at 2 M Br^- concentration, the energy density is 152 Wh l^{-1} versus 90 Wh l^{-1}). When the Br^- concentration reached 2.5 M, the battery's discharge capacity was able to achieve 130 Ah l^{-1}, with an impressive energy density of up to ~200 Wh l^{-1} (Supplementary Fig. 24).

With 1 M SANa in the electrolyte, our Zn/Br FBs achieved an energy density of 40 Wh l^{-1} and stable operation for over 500 cycles. (Fig. 3a and Supplementary Fig. 25a). By further increasing the SANa concentration in the electrolyte to 1.5 M, the battery's energy density reached an impressive 80 Wh l^{-1}. Moreover, long-term cycling tests at 40 mA cm^{-2} showed an EE of >80% for over 600 cycles (exceeding 80 days, or ~2,000 h; Fig. 3b and Supplementary Fig. 25b). The cycle life of this battery substantially outperforms traditional Zn/Br FBs (Supplementary Fig. 26) and surpasses the performance of most Br-based batteries (Supplementary Fig. 27). Increasing the concentration of SANa to 2 M achieved an energy density of ~120 Wh l^{-1}, which remained stable for 100 cycles (Supplementary Fig. 28). In addition, we verified the effect of KAc on the stability of the Zn anode by means of symmetric cell experiments. The results demonstrated that the battery operates stably, indicating that KAc has no observable effect on the Zn anode (Supplementary Fig. 29).

With a SPEEK membrane, traditional Zn/Br FB typically functioned only up to 30 cycles because of severe corrosion of the membrane by Br_2 (Fig. 3c). Compared to traditional Zn/Br batteries (assembled with corrosion-resistant polyolefin porous membranes or Daramic membrane[9,27]), our battery demonstrated a slightly lower EE (Supplementary Fig. 30a). The slope at the end of the discharge represents step 3 (in Fig. 2a), which accounts for 3.9% of the total capacity (Supplementary Fig. 30b). However, we are able to effectively address the corrosion issue and achieve a two-electron transfer reaction, making this minor EE expense acceptable. Testing the performance of our battery at different current densities and temperatures, we found that, as the current density increased from 20 mA cm^{-2} to 100 mA cm^{-2}, the coulombic efficiency (CE) rose from 94% to 98% while the voltage efficiency (VE) dropped from 90% to 70% (Fig. 3d). The enhancement in CE can be ascribed to the rise in current density, the shortening of charging and discharging times, and the alleviation in electrolyte crossover. At the same time, the decrease in VE is a result of the intensified electrochemical polarization. As the temperature increased, the CE dropped from 97% at 20 °C to 92% at 60 °C, while the VE increased from 80% at 20 °C to 90% at 60 °C (Supplementary Fig. 31). The decline in CE is primarily attributed to the intensified crossover at elevated temperatures, whereas the improvement in VE stems from the enhancement of electrochemical kinetics. It is worth mentioning that the battery can operate stably for over 80 cycles at 60 °C. However, the failure of the battery is not due to material instability, but rather due to the rapid migration of water at high temperatures, leading to drying on one side (Supplementary Fig. 32). In addition, FBs using polyolefin porous membranes can also exhibit high cycling stability, further demonstrating the wide applicability of our design (Supplementary Fig. 33).

To further demonstrate the practical prospect of our Zn/Br FB, we built a battery system by connecting 30 single cells of 1,900 cm^2 in series and equipping the stack with our own battery management system (BMS; Fig. 3e,f). With a zinc plating areal capacity of 60 mAh cm^{-2}, the system was evaluated at constant powers of 2.5 kW, 4 kW and 5 kW. The output energy of our system reached ~5.0 kWh, with the EE still at ~78% (Fig. 3g). The charging platform was at ~55–57 V, and the discharging platform at ~46–48 V. When the areal capacity of the zinc plating was increased to 80 mAh cm^{-2}, the output energy of the system was

https://doi.org/10.1038/s41560-025-01907-5

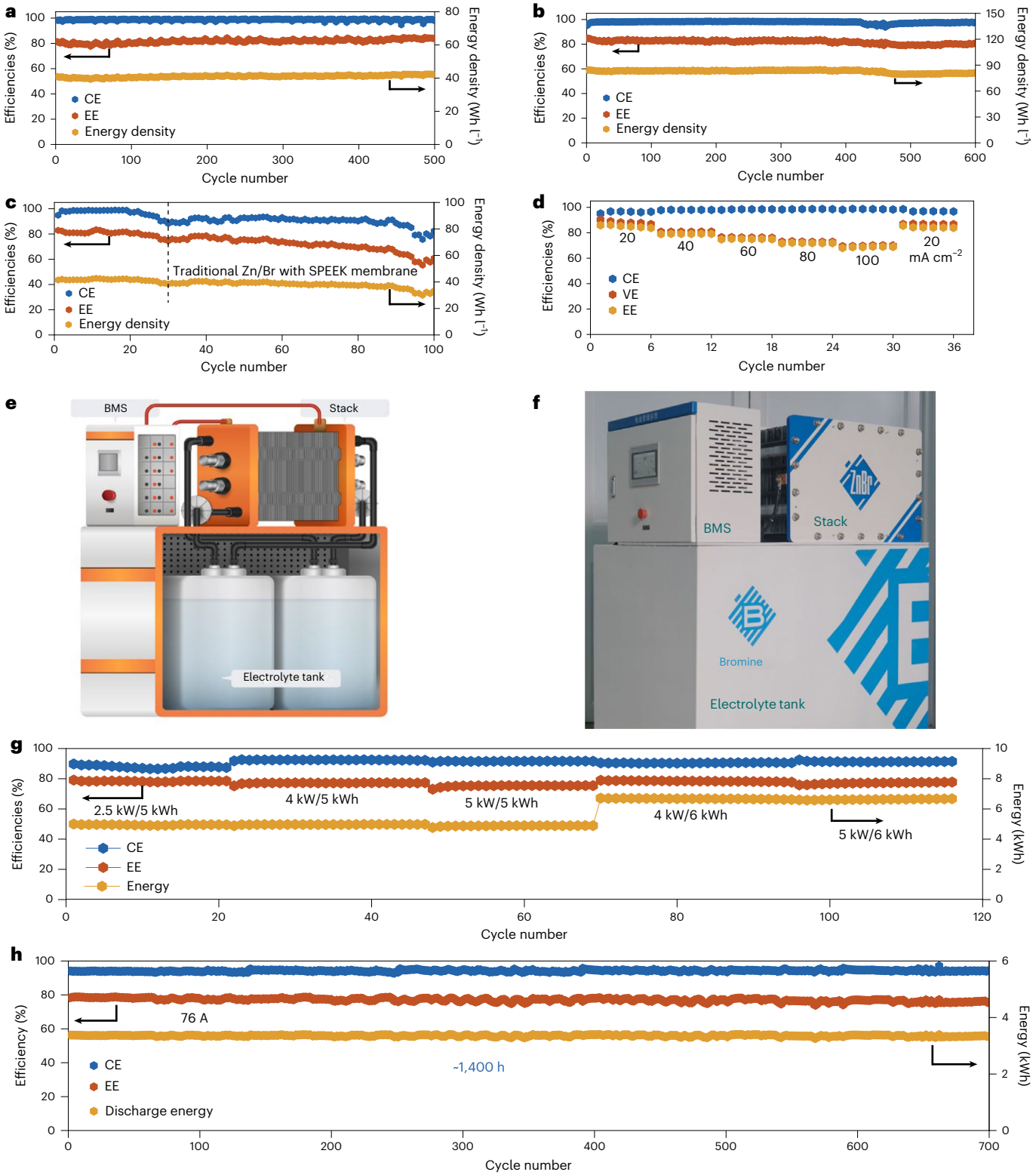

Fig. 3 | Single Zn/Br FB and scaled-up systems using our designed electrolytes outperform conventional systems. a,**b**, Long-term cycling test of a FB at 40 mA cm^{-2} with the following electrolytes: 1 M $ZnBr_2$ + 1 M SANa + 2 M KAc + 2 M KBr (**a**); 1 M $ZnBr_2$ + 1.5 M SANa + 1.5 M KAc + 2 M KBr (**b**). The results showed it was stable for >600 cycles with a lifespan of >80 days. **c**, The cycling performance of a conventional Zn/Br FB assembled with a SPEEK membrane and a regular Zn/Br electrolyte (1 M $ZnBr_2$ + 3 M KCl + 0.3 M MEP) deteriorated rapidly because SPEEK is not resistant to Br_2 corrosion. **d**, Battery performance of our single Zn/Br FB at different current densities (from 20 mA cm^{-2} to 100 mA cm^{-2}). **e**, Schematic diagram of the internal structure of the battery system, with the stack, electrolyte and BMS all marked in the diagram. **f**, Photograph of a battery system assembled using our electrolyte. The stack was composed of 30 single cells with an electrode area of 1,900 cm^2 connected in series and equipped with an in-house BMS. **g**, Performance of the assembled battery system under various powers ranging from 2.5 kW to 5 kW, with the maximum output energy greater than 6.6 kWh. The electrolyte composition was 1 M $ZnBr_2$ + 1 M SANa + 2 M KAc + 2 M KBr, and a volume of 145 l each was used for positive and negative sides. **h**, The stack underwent long-term operation testing at a current density of 40 mA cm^{-2}. The results indicate that the stack's cycle life exceeded 700 cycles (~1,400 h).

https://doi.org/10.1038/s41560-025-01907-5

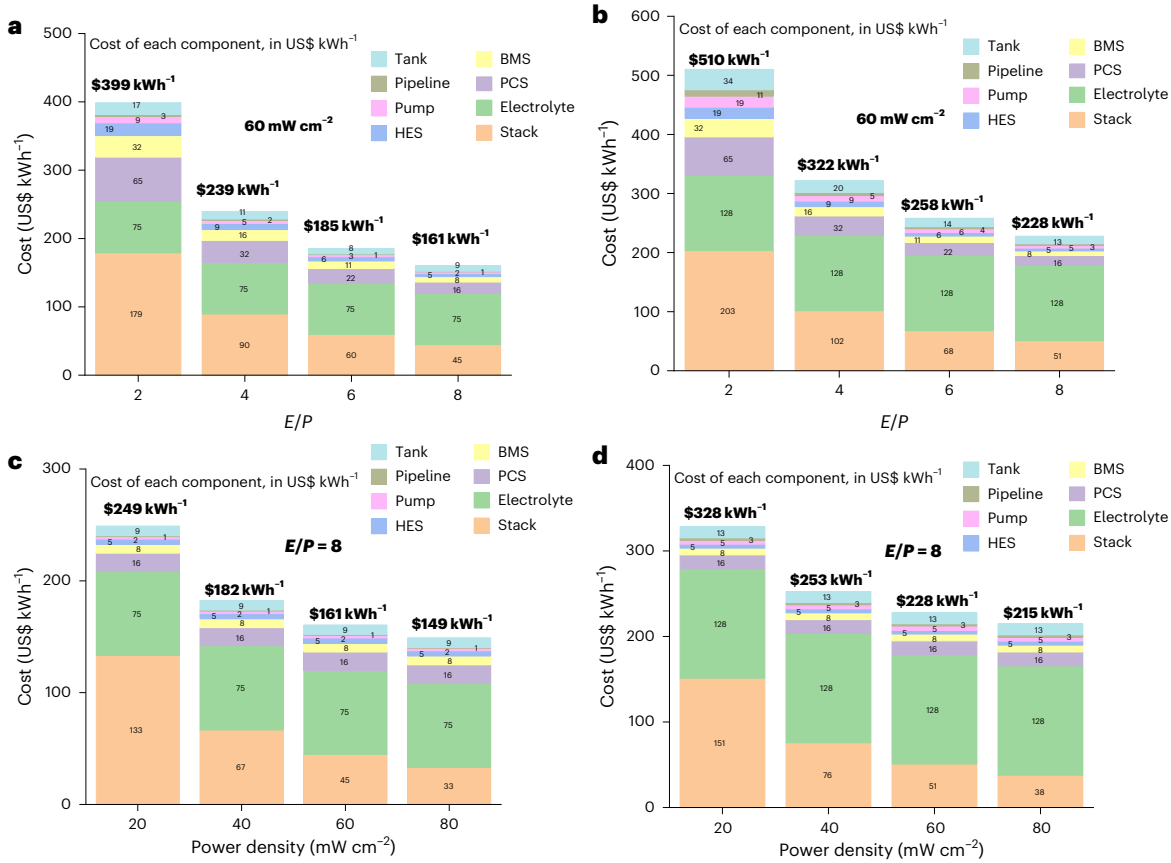

Fig. 4 | The ultralow-corrosion Zn/Br FB was more cost-effective than a traditional Zn/Br FB in most application modes. a,**b**, Cost calculation as a function of discharge duration (energy to power, *E*/*P*) at 60 mW cm^{-2} based on current performance, showing that our corrosion-resistant Zn/Br FB (**a**) costs less than the traditional Zn/Br FB (**b**). HES, heat exchange system; BMS, battery management system; PCS, power conversion system. Our system eliminates complexing agents such as MEP and expensive corrosion-resistant membrane materials, pipelines and electrolyte tanks. The two-electron transfer in our system reduces the number of redox species and thus the cost of the electrolyte. **c**,**d**, Cost calculation at different power densities (ranging from 20 mW cm^{-2} to 80 mW cm^{-2}) for our system (**c**) and the traditional Zn/Br FB (**d**) with *E*/*P* = 8. At constant *E*/*P*, improving the power density of the system substantially reduced the size of the stack and the amount of related materials used, thereby substantially reducing costs. See Supplementary Tables 2–13 for detailed cost calculations.

~6.6 kWh with an EE of ~78%. The stack was also subjected to cycling performance tests at a current density of 40 mA cm^{-2} (Fig. 3h and Supplementary Fig. 34). The results indicate that the stack can operate stably for over 700 cycles, with a total runtime of ~1,400 h. The outstanding performance of our system fully demonstrates the practicality and reliability of both the chemical reaction and the battery design. More importantly, we have successfully translated innovative ideas from the laboratory into real-system applications, substantially enhancing the credibility of this prospect.

Corrosion resistance test

To demonstrate the effectiveness of the Br_2 scavenger in mitigating the corrosive effects of Br_2 in the electrolyte, we assessed key materials before and after 500 cycles (corresponding to Fig. 3a), including the electrolyte, the SPEEK membrane, bipolar plates and electrodes, focusing on morphology, chemical properties and electrochemical behaviour. No substantial morphological changes were observed in any key materials (Supplementary Fig. 35). In contrast, conventional Br-based electrolytes led to corrosion in key materials (Supplementary Figs. 35 and 36)[28,29]. Advanced characterizations (inductively coupled plasma optical emission spectrometry (ICP-OES), CV, Raman and mass spectrometry) showed no notable changes in the electrolyte's concentration, composition or electrochemical behaviour (Supplementary Fig. 37). The SPEEK membrane showed excellent stability, with only a minor conductivity decrease due to Zn^{2+} ions occupying sulfonate groups (Supplementary Fig. 38). The results from stack cycling (corresponding to Fig. 3h) matched those from single-cell tests, confirming the electrolyte's low corrosiveness (Supplementary Figs. 39–41).

Techno-economic analysis of the ultralow-corrosion Zn/Br FB

The electrolyte cost per kilowatt-hour of our ultralow-corrosion Zn/Br FB (US$75 kWh^{-1}) was much lower than that of a traditional Zn/Br FB (US$128 kWh^{-1}), because it avoids expensive complexing agents[30,31] such as MEP, and the two-electron transfer reaction reduces the quantity of redox species (Fig. 4a,b and Supplementary Tables 2–13). Furthermore, the less corrosive electrolyte also substantially lowered the cost of the stack and auxiliary equipment, because there was no longer a need for corrosion-proof membranes, pumps and tanks. Compared to the traditional Zn/Br FB (cost of US$510 kWh^{-1}), our designed system (energy to power of *E*/*P* = 2; 60 mW cm^{-2}) was projected to cost US$399 kWh^{-1}. However, the battery stack still accounted for ~40–50% of this. Because the stack cost is closely related to discharge duration, we studied how the cost changes with discharge duration (*E*/*P* = 2–8). If the discharge duration of the system could be extended to *E*/*P* = 8 for instance, the cost of the system could be further reduced to US$161 kWh^{-1}. The cost of the stacks would also drop to less than 30% (Fig. 4a). For an *E*/*P* = 8 design, increasing the power density to 80 mW cm^{-2} would bring the

cost down further to approximately US$149 kWh^{-1} (Fig. 4c), and the cost gap with the traditional Zn/Br FB (US$215 kWh^{-1}) (Fig. 4d) would be mainly in the electrolyte. Therefore, our Zn/Br battery with a long discharge duration promises to be a low-cost and corrosion-resistant alternative for large-scale energy storage applications.

Conclusions

In summary, we have reported a chemical reaction for next-generation bromine FBs. Introducing SANa as a scavenger into the electrolyte effectively reduces the concentration of free Br_2 to ~7 mM. Reducing corrosive and volatile free Br_2 in this way substantially improves battery stability and reduces costs, because corrosion-proof materials are no longer needed. Compared with traditional single-electron transfer reactions (Br^-/Br_2), the two-electron transfer process (Br^-/Br–SANa) in our reaction greatly improves the energy density of the battery. When combined with a Zn anode, we obtained a high-energy-density, ultralow-corrosion Zn/Br FB. Our single battery was stable for >600 cycles and had an EE of over 80% at 40 mA cm^{-2}. Furthermore, the integrated 5-kW system assembled using the reaction demonstrated an output energy of ~6.6 kWh, an EE of 78% and a remarkable cycle life of over 700 cycles (or ~1,400 h). Our work shows that it is feasible to design mild, long-life and high-energy-density Br-based batteries for grid-scale applications.

Methods

Chemical reagents and materials

All commercial reagents for single battery tests and characterization were obtained from Aladdin and used as received without further purification. The reagents for the battery system test were purchased from Nantong Reform Chemical. Nafion 115 was purchased from Dupont. The SPEEK membrane was prepared according to our previous work[32]. The Daramic membrane was purchased from Polypore (Shanghai) Membrane Products. The carbon felt electrode was purchased from Liaoyang J-Carbon Materials. All electrolytes were prepared with deionized (DI) water.

Electrochemical measurements

The CV tests were performed using a typical three-electrode system. A 3-mm-diameter Pt electrode was used as the working electrode unless specified otherwise. The working electrode was polished with Al_2O_3 powder and rinsed with DI water. A saturated calomel electrode (SCE, 0.242 V versus standard hydrogen electrode (SHE)) and a graphite rod were used as reference and counter electrodes, respectively. All electrochemical measurements were performed on a Gamry Multichannel System installation.

Electrochemical kinetics calculations

The electron transfer rate constants (k_0) were calculated using the following equation[33]:

$$I = 0.227nFACk_0 \exp\left[-\frac{\alpha nF}{RT}(E - E_0)\right] \quad (7)$$

Here, n is the electron transfer number, F is the Faraday constant, A is the electrode area, C is the concentration of active species, α is the charge transfer coefficient, F is the Faraday constant, R is the gas constant, E is the peak potential and E_0 is the equilibrium potential.

The chemical reaction rate constant (k') was calculated by the following equation:

$$I_{cat} = nFAC_R^*(Dk'C_Z^*)^{1/2} \quad (8)$$

Here, I_{cat} is the peak oxidation current from CV measurements, C_R^* is the initial concentration of Br^-, D is the diffusion coefficient and C_Z^* is the initial concentration of SANa.

Thermodynamics calculations

The chemical equilibrium constants (K_1) of amino compounds (Ns) reacting with Br_2 were calculated according to

$$Ns + Br_2 \Longleftrightarrow H^+ + Br^- + BrNs \quad (9)$$

$$K_1 = \frac{[H^+][Br^-][BrNs]}{[Ns][Br_2]} \quad (10)$$

$$\log K_1 = \log[H^+] + \log[Br^-] + \log[BrNs] - \log[Ns] - \log[Br_2] \quad (11)$$

The initial concentrations of Ns and Br_2 were known and were set to the same value. The equilibrium concentrations of BrNs and Br^- were obtained from the pH change, that is, the amount of protons generated. Because the proportion of Br_2 hydrolysis was extremely low (for the 10 mM Br_2 solution, the proportion is less than 3%), its contribution to the Br^- and H^+ concentration after achieving reaction equilibrium could be ignored. Therefore, the remaining concentration of [Br_2] after the reaction was almost the same as the remaining concentration of [Ns]; meanwhile, the concentrations of generated [BrNs] and Br^- were the same.

$$\log\frac{[Br_2]}{[BrNs]} = -\frac{1}{2}pH - \frac{1}{2}\log K_1 \quad (12)$$

After adding acetate (Ac^-) as the buffer, the chemical equation was changed to the following form:

$$Ns + Br_2 + Ac^- \Longleftrightarrow HAc + Br^- + BrNs \quad (13)$$

$$K_2 = \frac{[HAc][Br^-][BrNs]}{[Ns][Br_2][Ac^-]} \quad (14)$$

Combined with the dissociation constant of HAc (K_{HAc}, 1.8×10^{-5} M^{-1}), the chemical equilibrium constants K_2 can be calculated as follows:

$$K_{HAc} = \frac{[H^+][Ac^-]}{[HAc]} \quad (15)$$

$$K_2 = \frac{K_1}{K_{HAc}} \quad (16)$$

$$\log\frac{[Br_2]}{[BrNs]} = -\frac{1}{2}pH - \frac{1}{2}\log K_2 + 2.38 \quad (17)$$

In situ Raman spectroscopy and SERS detection

Raman spectra were collected on the quartz tub with a Raman–AFM (atomic force microscope) combination (Nano Wizard Ultra Speed and inVia Raman) using a 532-nm laser. During the charging and discharging process, Raman signals were collected every 2 min. For the in situ SERS analysis of the electrode, a typical three-electrode system was adopted with Au (radius = 1 mm) as the working electrode, which was placed in KCl solution to achieve a rough surface. Raman spectra were collected using a 632-nm laser.

Mass spectroscopy

Mass spectroscopy was performed using a liquid chromatography–mass spectroscopy (time-of-flight high-resolution, Q-TOF 6540) combination. The mobile phase was DI water to prevent side reactions with the electrolyte. Negative-ion mode was used to detect anions in the electrolytes.

Infrared spectroscopy

For infrared spectroscopy measurements, the SPEEK membrane was pressed onto the surface of a diamond detector. The SPEEK membrane was then processed by vacuum freeze-drying after being immersed in the solution. Infrared spectroscopy was performed using a Thermo Fisher Scientific Fourier transform infrared spectrometer (Nicolet iS50) using the attenuated total reflectance method. The infrared spectra were collected 32 times after background subtraction.

^{1}H NMR measurement

The NMR spectrum was obtained using a 400-MHz NMR spectrometer (Bruker Avance III). DMSO-d_6 was used as the solvent due to the strong hydrogen–deuterium exchange in the amino group for water and other proton solvents. The solution of Br–SANa in DMSO-d_6 has to be tested immediately or it will react with the DMSO-d_6.

Morphological measurement

For the super-depth surface profile measurement, the raw current collector and the cycling one were tested, respectively. Surface fluctuations were evaluated using a super-depth surface profile microscope (VK-8550) with a magnification of ×400. The HTSCRN mode was used for height data collection, and the solid mode for three-dimensional imaging. The morphology of the carbon felt and membrane were detected by scanning electron microscopy (JSM-7800F and SUI510 instruments).

UV spectroscopy

For the UV spectroscopy measurements, the Br_2 extracted by carbon tetrachloride (CCl_4) was tested in a quartz cell (1-cm thickness) with an absorbance peak of 415 nm. Pure CCl_4 was used for the reference cell. UV spectra data were recorded using a UV–vis spectrometer (TU-1901, Beijing Purkinje General Instruments) with a range of ~300–600 nm.

The amount of Br_2 extracted by CCl_4 is consistent with that in the aqueous layer (Supplementary Fig. 42). Due to the dissociation equilibrium of Br–SANa in the aqueous phase ($Br–NH–SO_3^- + HAc + Br^- \rightarrow Br_2 + NH_2\text{-}SO_3^- + Ac^-$), the concentration of Br_2 after extraction remains almost unchanged, considering the large amount of Br–SANa in the solution. Because the distribution coefficient is close to 1, the Br_2 concentration in the CCl_4 layer is identical to the initial free Br_2 concentration in the aqueous phase. It should be noted that Br_2 has a low solubility in water, and the distribution coefficient between CCl_4 and water can reach 29. However, due to the presence of a large amount of Br^- in the solution, which has a co-solvent effect on Br_2, the distribution coefficient is substantially reduced to 1.

Degree of sulfonation measurement

The SPEEK membrane was freeze-dried for 6 h and cut into pieces for the NMR tube. After being fully dissolved, using DMSO-d_6 as the solvent, it was then used for ^{1}H NMR detection. The degree of sulfonation (DS) of the SPEEK membrane was calculated according to the following equation[34]:

$$\frac{\mathrm{DS}}{12-2\mathrm{DS}} = \frac{A_{\mathrm{H_1}}}{\sum A_{\mathrm{H_N}}} \tag{18}$$

where $A_{\mathrm{H_1}}$ represents the integrated peak area of the signal corresponding to the *ortho*-position H peak of -SO_3H, and $\sum A_{\mathrm{H_N}}$ represents the integration area of all the other aromatic hydrogens.

Permeability measurement

The permeability test was conducted using a diffusion cell with an effective diameter of 1.7 cm, with a membrane separating the two compartments. A 900-μm Daramic membrane was used for the traditional Zn/Br electrolyte and a SPEEK membrane was used in our Zn/Br electrolyte. Each side was filled with 50 ml of the anolyte and catholyte, respectively, after the FB had been charged (26.8 Ah l^{-1}). To minimize concentration polarization, the solutions on both sides were continuously stirred. At regular intervals, 3-ml samples were withdrawn and extracted with CCl_4 to measure the concentration of active Br_2 species. After each sampling, an equal volume of fresh electrolyte was added to maintain a constant volume. The Br_2 concentration was determined using UV–vis spectrometry, and the concentration of Br–SANa was measured by adding 1 M HBr to the diluted solution to convert it to Br_2.

Zn^{2+} concentration measurement

The concentration of Zn^{2+} was determined using ICP-OES (Avio 550 Max instrument, PerkinElmer). First, 0.500 g of the electrolyte (1.488 g ml^{-1}) was diluted to 30.000 g with 2 wt% HNO_3, then 0.500 g of this diluted solution was further diluted to 30.000 g with 2 wt% HNO_3. The resulting solution, after two dilutions, was used for ICP-OES testing. The concentration of Zn^{2+} in the original electrolyte was calculated based on the Zn^{2+} test results from ICP-OES, combined with the atomic weight of Zn (65.38 g mol^{-1}).

Electrode preparation

Carbon felt was used as electrodes for both the cathode and anode of the FB. The carbon felt for the anode was not further treated. The carbon felt for the cathode was loaded with carbon nanotubes to improve its activity and conductivity. First, 1 g of carbon nanotubes was mixed with 0.1 g of PVDF and 400 g of *N*-methylpyrrolidone (NMP) and stirred overnight to prepare a slurry. The carbon felt, with an electrode area of 48 cm^2, was then soaked in the slurry for 10 s and dried in an oven at 80 °C for 24 h.

FB measurements

The FB was assembled by sandwiching the membrane between two carbon felts as cathode and anode, and clamped by two carbon-based current collectors. The carbon felt was cut to 6 × 8 cm^2 with a thickness of 5 mm, and the compressed ratio was ~30%. The SPEEK membrane (thickness of ~60 μm) designed by us was used for the battery test in a near-neutral environment, and Nafion 115 was used for the battery test in a strongly acidic environment. The volume of electrolytes on both sides was set to 60 ml. The electrolytes were pumped by a magnetic-drive pump and the flow rate was kept at ~70 ml min^{-1}. The FB test was carried out on a NEWARE battery test system (CT-4008T-5V12A), with constant capacity charging cutoff and voltage discharging cutoff (0.1 V). FBs operating at different temperatures were assessed in a constant-temperature chamber with a temperature range from 10 °C to 60 °C (ET-020L system, Shanghai ESPEC). The specific capacity (C) of the battery was calculated based on the catholyte volume using the following formula:

$$C = C_{\mathrm{discharge}}/V \tag{19}$$

The energy density was calculated based on the actual discharge energy of the battery under specific conditions and the volume of the catholyte. The calculation formula is as follows: $E = E_{\mathrm{discharge}}/VE_{\mathrm{discharge}}$ represents the energy output of the battery (Wh), V is the volume of the catholyte (L).

Stacks and battery system measurement

The 5-kW system was assembled by connecting 30 single cells in series, with an active area of 1,900 cm^2. Components such as bipolar plates, membrane materials and PVC frames were designed and processed by our group. The system was equipped with a BMS to detect the system temperature, electrolyte flow rate and other parameters. The system was charged and discharged under constant power. The charging cutoff was capacity and the discharge cutoff was 24 V. Two parallel tests of stacks were investigated to analyse the changes in stack materials before and after cycling. The pump power of the system was only 180 W, accounting for just 3.6% of the total power.

Computational methods

Density functional theory calculations were performed using the Gaussian 16 (ref. 35) package. For bond energy calculations, all structures were optimized at the B3LYP/def2-TZVP level, including the atom-pairwise dispersion (D3) correction[36,37] with Becke–Johnson[38] (BJ) damping, followed by a frequency calculation. For Gibbs free-energy calculations, the structures were first optimized with the B3LYP/6-31+G(d) calculation level, also including D3BJ correction, followed by a frequency calculation. The solvation energy was then calculated by the energy of M05-2X/6-31G(d) with the implicit universal water solvation model based on solute electron density (SMD)[39] minus the energy of M05-2X/6-31G(d) in vacuum. We added 1.89 kcal mol^{-1} for each 1 mol of molecules solvated from vacuum to liquid. A single-point energy calculation of each optimized structure was subsequently carried out at B3LYP/def2-TZVP[40] including D3BJ correction. The Gibbs free energy of each structure was the sum of the thermal correction to the Gibbs free energy from the frequency calculation, solvation energy and single-point energy.

Cost calculation

The calculation of future practical system costs was based on MW-class systems. All system costs were calculated based on a model stack consisting of 60 cells of 3,600 cm^2 connected in series, which was a mature stack design for our group. The electrode area of the stack on each side was 21.6 m^2 (3,600 $cm^2 \times 60$), and the number of stacks required per MW (N) was calculated as

$$N = 4629.62/P \tag{20}$$

where P is the power density (mW $cm^{-2}_{\text{electrode area}}$) at which the system operates. Details of all component costs are provided in Supplementary Tables 2–13.

To further reflect the practicality and commercial value of the system, we conducted a comprehensive cost analysis, including the stack, electrolyte, control system and auxiliary equipment. In addition to the price of key materials, the cost per kWh of the system was closely related to the operating mode, especially the power density and cycle duration. For stacks, as power density increased, the number of stacks required for a fixed power decreased substantially, which means a decrease in the demand for key materials such as membranes and electrodes. In addition, the extension of cycle duration could linearly increase the output energy of a single stack. The cost per kWh would thus also be notably reduced. Therefore, increasing the power density and extending the cycle duration are key factors to reduce system costs.

For a 1-MW system design, as the charging time increased from 2 h to 8 h, the system cost per kWh dropped substantially from US$399 kWh^{-1} to US$161 kWh^{-1} (Fig. 4a), with the main part of the cost reduction being for the stack (US$179 kWh^{-1} versus US$45 kWh^{-1}), which accounted for approximately half of the total cost.

Compared with the system we designed, the cost of the traditional Zn–Br FB system was much higher. This was because our electrolyte was cheaper (US$128 kWh^{-1} versus US$75 kWh^{-1}) due to the absence of expensive complexing agents such as MEP (Fig. 4a,b). Because our electrolyte system was less corrosive, key materials had lower corrosion-resistance requirements, such as membranes (SPEEK US$12.3 m^{-2} versus Daramic US$30 m^{-2}), pipelines, tanks and pumps. However, for Zn hybrid FBs, the cycle duration was limited by the Zn dendrite issue. It was necessary to suppress this by optimizing the electrolyte composition and electrode structure to extend the cycle duration.

Similarly, if the power density were increased from 20 mW cm^{-2} to 80 mW cm^{-2}, the cost of the system (1 MW/8 MWh) would drop from US$249 kWh^{-1} to US$149 kWh^{-1} (Fig. 4c). This cost reduction also mainly came from the substantial reduction in the stack cost (US$133 kWh^{-1} versus US$33 kWh^{-1}). According to our assumptions, if the power density of the system were greatly increased and the charging time of the system greatly increased in the future, the cost of the system could be expected to reduce to approximately US$150 kWh^{-1}, which is close to that of lithium-ion batteries.

Br-based battery cost comparison

Our comparison of Br-based battery performance included Ti-Br[41], [MV]Br_2-Br[42], (2HO-V)Br_2-Br[43], H-Br[44], AQDS-Br[45], 2,7-AQDS-Br[46] and Sn-Br[47]. Some systems had clearly indicated energy densities, but the energy densities (E) of the other systems were calculated based on the battery's specific discharge capacity (C) and the battery's average discharge voltage (V) according to

$$E = C \times V \tag{21}$$

E refers to the energy density of the battery (in units of Wh l^{-1}), C the specific capacity of the battery (in Ah l^{-1}) and V the average discharge voltage of the battery (in V).

Data availability

All relevant data are included in the paper and its Supplementary Information. Source data are provided with this paper.

References

1. Tang, L. Y., Lu, W. J. & Li, X. F. Electrolytes for bromine-based flow batteries: challenges, strategies and prospects. *Energy Stor. Mater.* **70**, 103532 (2024).
2. Mahmood, A., Zheng, Z. & Chen, Y. Zinc–bromine batteries: challenges, prospective solutions and future. *Adv. Sci.* **11**, 2305561 (2024).
3. Popat, Y. et al. Carbon materials as positive electrodes in bromine-based flow batteries. *ChemPlusChem* **87**, e202100441 (2022).
4. Futamata, M. & Takeuchi, T. Deterioration mechanism of the carbon-plastic electrode of the Zn-Br_2 battery. *Carbon* **30**, 1047–1053 (1992).
5. Saikia, I., Borah, A. J. & Phukan, P. Use of bromine and bromo-organic compounds in organic synthesis. *Chem. Rev.* **116**, 6837–7042 (2016).
6. Kim, R. et al. Ultrathin Nafion-filled porous membrane for zinc/bromine redox flow batteries. *Sci. Rep.* **7**, 10503 (2017).
7. Shakil, S. et al. Behavioral and neuronal effects of inhaled bromine gas: oxidative brain stem damage. *Int. J. Mol. Sci.* **22**, 6316 (2021).
8. Carel, R. S., Belmaker, I., Potashnik, G., Levine, M. & Blau, R. Delayed health sequelae of accidental exposure to bromine gas. *J. Toxicol. Environ. Health* **36**, 273–277 (1992).
9. Tang, L., Li, T., Lu, W. & Li, X. Reversible solid bromine complexation into $Ti_3C_2T_x$ MXene carriers: a highly active electrode for bromine-based flow batteries with ultralow self-discharge. *Energy Environ. Sci.* **17**, 3136–3145 (2024).
10. Zhu, F., Guo, W. & Fu, Y. Functional materials for aqueous redox flow batteries: merits and applications. *Chem. Soc. Rev.* **52**, 8410–8446 (2023).
11. Wei, C., Song, J., Wang, Y., Tang, X. & Liu, X. Recent development of aqueous multivalent-ion batteries based on conversion chemistry. *Adv. Funct. Mater.* **33**, 2304223 (2023).
12. Zhao, M. et al. A choline-based antifreezing complexing agent with selective compatibility for Zn–Br_2 flow batteries. *Small* **20**, 2307627 (2023).
13. Xu, C. et al. Practical high-energy aqueous zinc-bromine static batteries enabled by synergistic exclusion-complexation chemistry. *Joule* **8**, 461–481 (2024).
14. Djerassi, C. Brominations with *N*-bromosuccinimide and related compounds; the Wohl-Ziegler reaction. *Chem. Rev.* **43**, 271–317 (1948).
15. Choi, G. et al. Soft-hard zwitterionic additives for aqueous halide flow batteries. *Nature* **635**, 89–95 (2024).

16. Eraković, M., Cinčić, D., Molčanov, K. & Stilinović, V. A crystallographic charge density study of the partial covalent nature of strong N···Br halogen bonds. *Angew. Chem. Int. Ed.* **58**, 15702–15706 (2019).
17. Elroby, S. A. K., Noamaan, M. A. & Shibl, M. F. Quantum mechanical studies of the protonation and N-Br bond dissociation of the biologically important *N*-bromosuccinimide. *J. Mol. Struct. THEOCHEM* **915**, 93–97 (2009).
18. Basha, S. J. & Chamundeeswari, S. P. V. Quantum computational, spectroscopic and molecular docking studies of 5,5-dimethyl-hydantoin and its bromine and chlorine derivatives. *Chem. Data Collect.* **29**, 100461 (2020).
19. Panikar, S. S., Guirgis, G. A., Sheehan, T. G., Durig, D. T. & Durig, J. R. Infrared spectra, vibrational assignment, and ab initio calculations for *N*-bromo-hexafluoro-2-propanimine. *Spectrochim. Acta A. Mol. Biomol. Spectrosc.* **90**, 118–124 (2012).
20. Muthusubramanian, P. & Raj, A. S. Raman spectra of sodium sulphamate single crystal. *Can. J. Chem.* **61**, 2048–2052 (1983).
21. Chen, X. et al. Raman spectroscopic investigation of tetraethyl-ammonium polybromides. *Inorg. Chem.* **49**, 8684–8689 (2010).
22. Yang, C. et al. Aqueous Li-ion battery enabled by halogen conversion-intercalation chemistry in graphite. *Nature* **569**, 245–250 (2019).
23. Aguirre, C. M., Kaspar, T. R., Radloff, C. & Halas, N. J. CTAB mediated reshaping of metallodielectric nanoparticles. *Nano Lett.* **3**, 1707–1711 (2003).
24. Wang, H., Levin, C. S. & Halas, N. J. Nanosphere arrays with controlled sub-10-nm gaps as surface-enhanced Raman spectroscopy substrates. *J. Am. Chem. Soc.* **127**, 14992–14993 (2005).
25. Sandford, C. et al. A synthetic chemist's guide to electroanalytical tools for studying reaction mechanisms. *Chem. Sci.* **10**, 6404–6422 (2019).
26. Badalyan, A. & Stahl, S. S. Cooperative electrocatalytic alcohol oxidation with electron-proton-transfer mediators. *Nature* **535**, 406–410 (2016).
27. Tang, L. Y. et al. In situ vertically aligned MoS_2 arrays electrodes for complexing agent-free bromine-based flow batteries with high power density and long lifespan. *Adv. Energy Mater.* **14**, 2303282 (2024).
28. Biswas, S. et al. Minimal architecture zinc-bromine battery for low cost electrochemical energy storage. *Energy Environ. Sci.* **10**, 114–120 (2017).
29. Li, X., Xie, C., Li, T., Zhang, Y. & Li, X. Low-cost titanium-bromine flow battery with ultrahigh cycle stability for grid-scale energy storage. *Adv. Mater.* **32**, e2005036 (2020).
30. Eustace, D. J. Bromine complexation in zinc-bromine circulating batteries. *J. Electrochem. Soc.* **127**, 528–532 (1980).
31. Bryans, D., McMillan, B. G., Spicer, M., Wark, A. & Berlouis, L. Complexing additives to reduce the immiscible phase formed in the hybrid $ZnBr_2$ flow battery. *J. Electrochem. Soc.* **164**, A3342–A3348 (2017).
32. Yuan, Z. et al. Low-cost hydrocarbon membrane enables commercial-scale flow batteries for long-duration energy storage. *Joule* **6**, 884–905 (2022).
33. Waters, S. E., Robb, B. H. & Marshak, M. P. Effect of chelation on iron-chromium redox flow batteries. *ACS Energy Lett.* **5**, 1758–1762 (2020).
34. Robertson, G. P. et al. Casting solvent interactions with sulfonated poly(ether ether ketone) during proton exchange membrane fabrication. *J. Membr. Sci.* **219**, 113–121 (2003).
35. Frisch. M. J. et al. Gaussian 16 Rev. A.03 (Gaussian, 2016).
36. Grimme, S. Accurate description of van der Waals complexes by density functional theory including empirical corrections. *J. Comput. Chem.* **25**, 1463–1473 (2004).
37. Grimme, S., Ehrlich, S. & Goerigk, L. Effect of the damping function in dispersion corrected density functional theory. *J. Comput. Chem.* **32**, 1456–1465 (2011).
38. Johnson, E. R. & Becke, A. D. A post-Hartree-Fock model of intermolecular interactions: inclusion of higher-order corrections. *J. Chem. Phys.* **124**, 174104 (2006).
39. Marenich, A. V., Cramer, C. J. & Truhlar, D. G. Universal solvation model based on solute electron density and on a continuum model of the solvent defined by the bulk dielectric constant and atomic surface tensions. *J. Phys. Chem. B* **113**, 6378–6396 (2009).
40. Weigend, F. & Ahlrichs, R. Balanced basis sets of split valence, triple zeta valence and quadruple zeta valence quality for H to Rn: design and assessment of accuracy. *Phys. Chem. Chem. Phys.* **7**, 3297–3305 (2005).
41. Xu, Y., Xie, C., Li, T. & Li, X. A high energy density bromine-based flow battery with two-electron transfer. *ACS Energy Lett.* **7**, 1034–1039 (2022).
42. Wu, W., Luo, J., Wang, F., Yuan, B. & Liu, T. L. A self-trapping, bipolar viologen bromide electrolyte for redox flow batteries. *ACS Energy Lett.* **6**, 2891–2897 (2021).
43. Liu, W. et al. A highly stable neutral viologen/bromine aqueous flow battery with high energy and power density. *Chem. Commun.* **55**, 4801–4804 (2019).
44. Lin, G. et al. Advanced hydrogen-bromine flow batteries with improved efficiency, durability and cost. *J. Electrochem. Soc.* **163**, A5049–A5056 (2015).
45. Huskinson, B. et al. A metal-free organic-inorganic aqueous flow battery. *Nature* **505**, 195–198 (2014).
46. Abunaeva, L. et al. Successful charge-discharge experiments of anthraquinone-bromate flow battery: first report. *Energies* **15**, 7967 (2022).
47. Zeng, Y., Yang, Z., Lu, F. & Xie, Y. A novel tin-bromine redox flow battery for large-scale energy storage. *Appl. Energy* **255**, 113756 (2019).

Acknowledgements

This work was supported financially by the National Natural Science Foundation of China (grant no. 22525081 to X.L., 22209179 to C.X. and 22478379 to C.X.), the International Partnership Program of the Chinese Academy of Sciences (121421KYSB20210028 to X.L.), the Science and Technology Major Project of Liaoning Province (grant no. 2024JH1/11700011 to C.X.), the Strategic Priority Research Program of the Chinese Academy of Sciences (XDA0400201 to X.L.), Liaoning Binhai Laboratory (no. LBLD 202401) and the Liaoning Provincial Natural Science Foundation (2023-MS-010 to C.X.). We thank A. L. Chun of Science Storylab for critically reading and editing the manuscript. We thank Y. Song and C. Yuan at the Dalian Institute of Chemical Physics for their support in system assembly. We thank Z. Zhao at the Dalian Institute of Chemical Physics for his support with SERS testing. We thank C. Mu at the Dalian Institute of Chemical Physics for his support with theoretical calculations.

Author contributions

Y.X., C.X. and X.L. conceived the projects and designed the experiments. Y.X. and C.X. conducted the electrochemical tests and material characterizations. T.L. conducted the theoretical calculations. Y.X., C.X., Z.P. and X.L. co-wrote and revised the paper. C.X. and X.L. supervised the work and discussed the results.

Competing interests

The authors declare no competing interests.

Additional information

Supplementary information The online version contains supplementary material available at https://doi.org/10.1038/s41560-025-01907-5.

Correspondence and requests for materials should be addressed to Congxin Xie or Xianfeng Li.

Peer review information *Nature Energy* thanks Yuan Chen and the other, anonymous, reviewer(s) for their contribution to the peer review of this work.